Ultrahigh Energy Absorption Multifunctional Spinodal Nanoarchitectures

Anna Guell Izard, Jens Bauer, Cameron Crook, Vladyslav Turlo, and Lorenzo Valdevit*

Nanolattices are promoted as next-generation multifunctional high-performance materials, but their mechanical response is limited to extreme strength yet brittleness, or extreme deformability but low strength and stiffness. Ideal impact protection systems require high-stress plateaus over long deformation ranges to maximize energy absorption. Here glassy carbon nanospinodals, i.e., nanoarchitectures with spinodal shell topology, combining ultrahigh energy absorption and exceptional strength and stiffness at low weight. Noncatastrophic deformation up to 80% strain, and energy absorption up to one order of magnitude higher than for other nano-, micro-, macro-architectures and solids, and state-of-the-art impact protection structures are shown. At the same time, the strength and stiffness are on par with the most advanced yet brittle nanolattices, demonstrating true multifunctionality. Finite element simulations show that optimized shell thickness-to-curvature-radius ratios suppress catastrophic failure by impeding propagation of dangerously oriented cracks. In contrast to most micro- and nano-architected materials, spinodal architectures may be easily manufacturable on an industrial scale, and may become the next generation of superior cellular materials for structural applications.

Over the past decades, the development of architected materials has seen dramatic progress, with the overarching goal of developing the next generation of multifunctional high-performance materials.[1] Optimal design of the lattice topology enables combinations of classically mutually exclusive properties,[2] such as low density, high strength, high stiffness, high damping, and high deformability. Recently, high-resolution additive manufacturing approaches have been used to fabricate architected materials with topological features at the nanoscale, enabling exploitation of size-effects to achieve order-of-magnitude increases in strength over macroarchitected materials.[2]

The ideal material for multifunctional impact protection systems possesses high strength (to resist penetration) and high energy absorption capability (to protect from blast) at low weight. The energy which a material absorbs under deformation is defined as the integral of the corresponding stress–strain response. High-stress plateaus over a long strain regime maximize energy absorption. However, the strongest existing monolithic materials are generally brittle, with extremely low failure strains; conversely, those with extensive near-constant stress plateaus under deformation, like ductile metals, typically have relatively low strength and high weight. Today, cellular materials and structures such as foams, honeycombs, and fiber composite tubes provide the most efficient compromise.[3] Unlike in monolithic solids, localized fracture, instability, and friction facilitate progressive failure with fairly high stress plateaus. Clearly, nanoarchitected materials have the potential to take advantage of those same effects, which could be further amplified by the extreme constituent material strength at the nanoscale.

So far, lightweight nanoarchitected materials have mostly been designed for either high deformability[4–7] or high strength,[8–10] with true multifunctionality remaining a major challenge. Elastic beam buckling allows repeatable recoverability from large-strain compression in low density lattices,[6,11,12] providing high damping capability.[7] However, those buckling mechanisms and high imperfection sensitivity cause low specific strength,[2] i.e., the strength-to-weight ratio, and therefore poor energy absorption during deformation. Conversely, more-dense nanoscale truss designs efficiently exploit material strengthening size-effects, and hence possess high specific strength; however, brittleness with catastrophic failure at low strains limits the energy absorption capability. The sharply intersecting beams typically concentrate high stresses at the lattice nodes,[6,13] providing a path for catastrophic crack propagation. Plate-based designs are notably stronger and stiffer than their beam-based counterparts,[14,15] potentially alleviating some of the above challenges; however, they are still similarly affected by stress concentrations.

Shell-based architected materials are comprised of smoothly interconnected surfaces with drastically reduced stress concentrations compared to beam-based designs and may allow to better combine high strength and deformability.[16] Shell-based topologies have a mean curvature close to zero everywhere, which facilitates a uniform strain distribution upon loading.[16,17] This unique topological feature has also been shown to impart them good strength and stiffness.[13,16,18]

A. Guell Izard, Dr. J. Bauer, Prof. L. Valdevit
Department of Mechanical and Aerospace Engineering
University of California, Irvine
Irvine, CA 92697, USA
E-mail: valdevit@uci.edu
C. Crook, Dr. V. Turlo, Prof. L. Valdevit
Department of Materials Science and Engineering
University of California, Irvine
Irvine, CA 92697, USA

The ORCID identification number(s) for the author(s) of this article can be found under https://doi.org/10.1002/smll.201903834.

**ADVANCED
SCIENCE NEWS**
www.advancedsciencenews.com
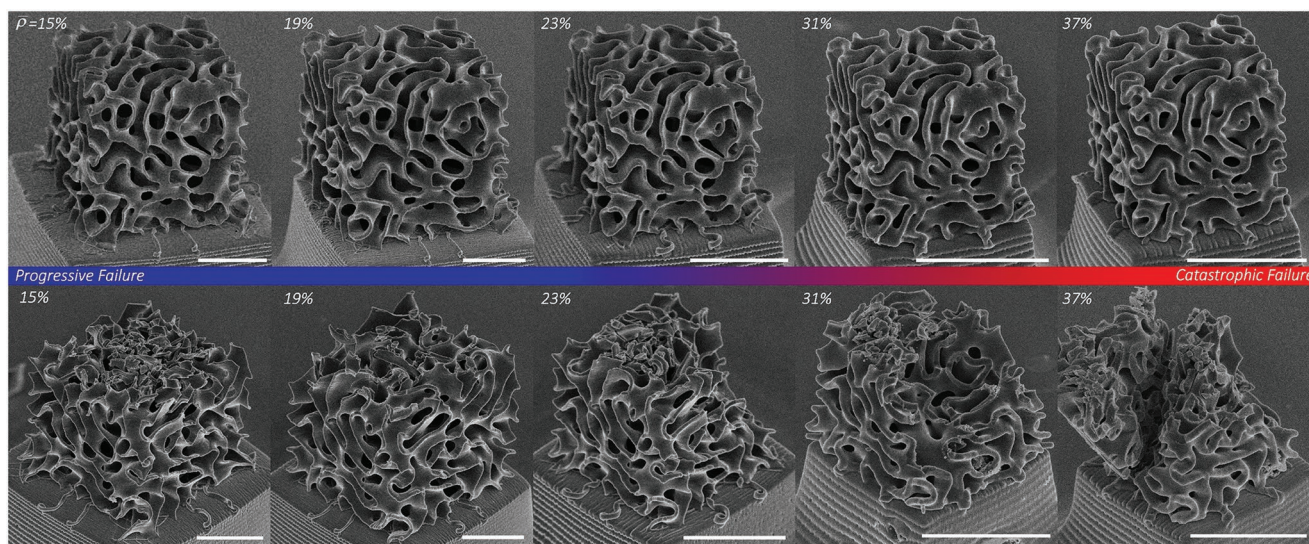
NANO · MICRO
small
www.small-journal.com

Figure 1. Glassy carbon nanospinodals with different relative densities ($\bar{\rho}$) were manufactured via two-photon direct laser writing (TPP-DLW) and subsequent pyrolysis at 900 °C. Top and bottom images show the structures before and after initial failure, respectively, showing the transition from a progressive to a catastrophic failure mechanism. Scale bars are 5 µm.

A particular class of shell-based architectures are spinodal topologies, which can be produced by spinodal decomposition of two phases followed by removal of one phase, coating of the interface and subsequent removal of the second phase.[19] Compared to periodic designs, their stochastic nature provides decreased imperfection sensitivity as well as fully isotropic behavior, while still offering near-uniform strain distribution upon loading.[18,20] Thus, shell-based spinodal topologies are ideal candidates for combining high energy absorption capability, strength, and stiffness at low weight.

In this paper, we present multifunctional glassy carbon nanospinodals, which combine ultrahigh energy absorption capability and exceptional strength. The spinodal shell topology is generated by extracting the phase-interface of a numerically simulated spinodally decomposed solid. Using two-photon direct laser writing and subsequent pyrolysis, we manufacture glassy carbon spinodal structures with relative densities ($\bar{\rho}$), i.e., the constituent material volume fraction, of 15–40% and characteristic feature sizes of 170 nm (**Figure 1**). We show progressive, noncatastrophic failure under uniaxial compression with specific energies absorption up to 200 kJ kg^{-1}. This is up to one order of magnitude higher than for other nano-, micro-, and macro-scale architected materials and most state of the art impact protection structures.[21] At the same time, we measure strengths and Young's moduli on par with the most advanced, yet brittle nanolattices,[8–10] demonstrating true multifunctionality. Finite element simulations indicate that optimized shell-based spinodal topologies prevent catastrophic failure under compression by impeding propagation of cracks that are aligned with the loading direction. This enables progressive failure, with elongated high-stress plateaus which cannot be realized with beam-based lattices. Beyond the evident mechanical advantages over previously reported nanolattices, this finding is of significant general relevance for cellular materials. While manufacturing constraints hinder widespread industrial application of lattice materials, shell-based nanospinodals may be manufacturable on an industrial scale and could soon replace traditional foam materials.

Glassy carbon nanospinodals show a distinct transition from progressive layer-by-layer-type failure to catastrophic brittle fracture when the relative density increases above ≈25% (Figures 1 and 2). **Figure 2**a shows compressive stress–strain responses for the progressive relative density regime, where high plateau stresses are maintained from initial failure up to strains as high as 80%. Deformation and failure thereby initiate at the top surface of the specimens, which represents the weakest link due to the free surface, and then propagate through the specimen, toward the constrained bottom face. With increasing $\bar{\rho}$, curves become more jagged with more pronounced local stress drops; however, failure still occurs in a noncatastrophic layer-by-layer fashion (Movie S1, Supporting Information). By contrast, specimens with $\bar{\rho} > 25\%$ are mostly limited to linear elastic behavior followed by catastrophic shear fracture or vertical splitting of the entire structure, with maximum strains around 8% (Figure 2b) (Movies S2 and S3, Supporting Information).

Progressive failure dramatically increases the energy absorption capability of glassy carbon nanospinodals compared to catastrophic failure. Figure 2c shows the absorbed energy as a function of the relative density. In the catastrophic regime, we measure energy absorptions per unit volume (U) of 25–39 MJ m^{-3} at relative densities of 31–40%, which translates to specific energy absorptions ($\bar{U}$) of 60–80 kJ kg^{-1} and an exponential scaling of U with the relative density ($U \sim \bar{\rho}^{1.67}$). In the progressive regime, the absorbed energy scales nearly linearly with the relative density ($U \sim \bar{\rho}^{0.95}$), meaning $\bar{U}$ does not deteriorate for the lowest $\bar{\rho}$ structures, which show the smoothest deformation behavior. Measured energy absorption values of 36–58 MJ m^{-3} at relative densities between 15% and 23% correspond to $\bar{U}$ of 170–192 kJ kg^{-1}, which is a threefold increase compared to the nanospinodals in the catastrophic regime.

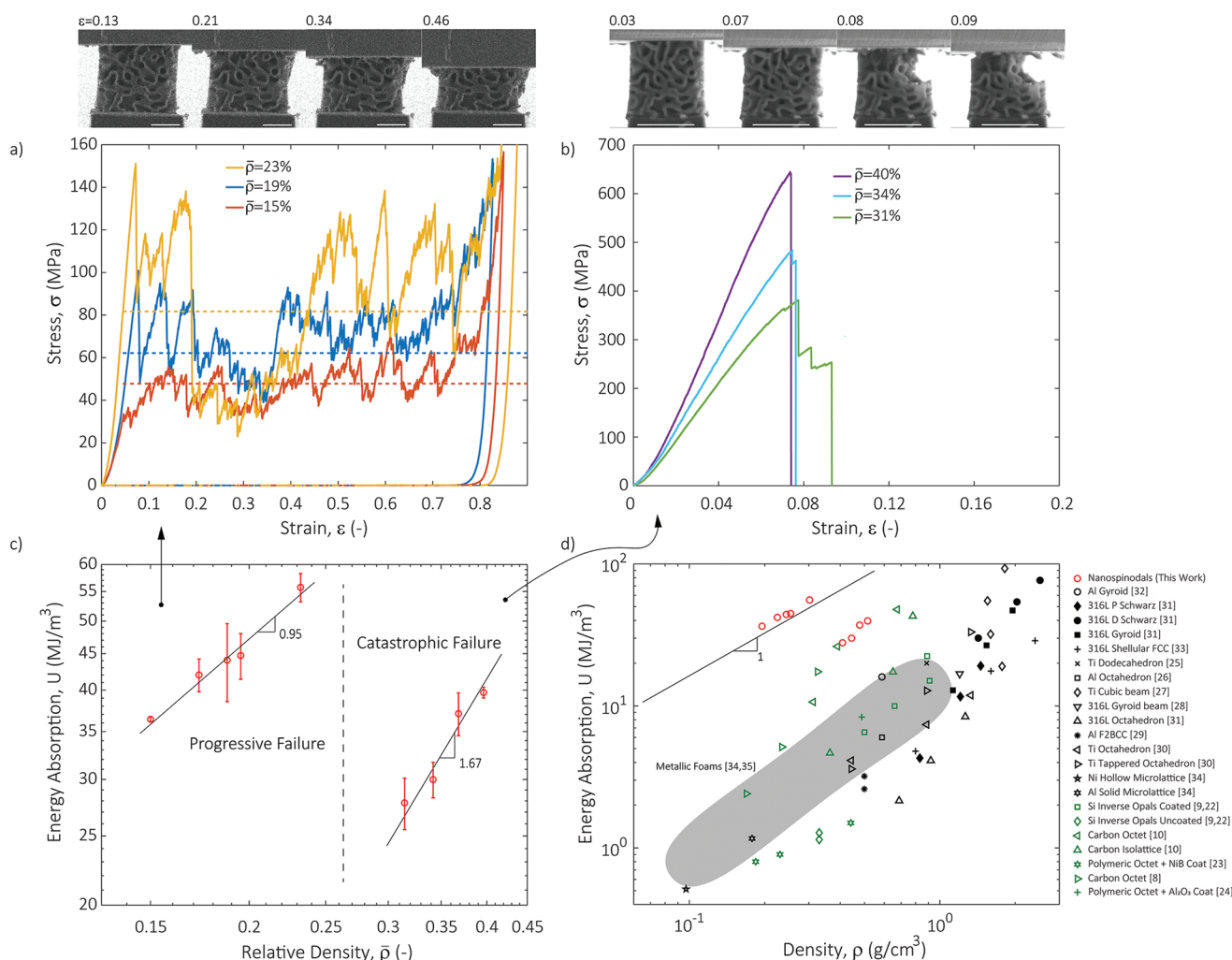The energy absorption capability of progressively failing glassy carbon nanospinodals substantially exceeds

ADVANCED
SCIENCE NEWS
www.advancedsciencenews.com

NANO · MICRO
small
www.small-journal.com

Figure 2. Compressive stress–strain curves of glassy carbon nanospinodals with a) progressive and b) catastrophic failure; dashed lines indicate the plateau stress, SEM images correspond to $\overline{\rho} = 19\%$ and $\overline{\rho} = 34\%$, scale bars are 5 μm. c) Energy absorption versus relative density. d) Comparison of the energy absorption with metallic foams,[34,35] nanolattices,[8–10,22–24] large-scale beam-,[25–31] and shell-based lattices.[31–34]

that of any other 3D architected material (Figure 2d). We measure 3–20 times increased specific energy absorption compared to the most advanced nanolattices,[8–10,22–24] as well as larger-scale beam-,[25–31] and shell-based architected materials.[31–34] Compared to metal foams, our nanospinodals show up to an order of magnitude increase in energy absorption capability.[34,35] While spinodal topologies are fully isotropic, the $\overline{U}$ values measured herein are 2–6 times higher than those of highly anisotropic nanohoneycombs[23,24,36] and state-of-the-art impact protection structures like aluminum-, glass fiber-, and Kevlar composite-tubes, and comparable to those of carbon/peek tubes, which have the highest $\overline{U}$ on the market.[21] Remarkably, despite the ceramic constituent material, the energy absorption efficiency (η), i.e., the ratio of energy absorption (U) to compressive strength (σ_c),[37] of our nanospinodals is as high as $\eta = 0.55$, comparable to the highest known values for metallic[34] and plastic foams (Figure S4a, Supporting Information).[37]

While possessing superior energy absorption capability, glassy carbon nanospinodals are at the same time ultrastrong

and ultrastiff (**Figure 3**). Compressive strength-to-density ratios are on par with or even above those of beam-based glassy carbon nanolattices (Figure 3a), which are the strongest reported architected materials and were synthesized by the same fabrication route as applied here.[8,10] The same is true for the compressive stiffness (Figure 3b). Correlating with the two distinct failure modes (progressive and catastrophic), both compressive strength (σ_c) and stiffness (E_c) of glassy carbon nanospinodals show two distinct scaling behaviors with $\overline{\rho}$. In the progressive (low $\overline{\rho}$) range, σ_c and E_c scale with $\overline{\rho}$ as $\sigma_c \sim \overline{\rho}^{1.34}$ and $E_c \sim \overline{\rho}^{1.43}$, respectively. This is in excellent agreement with finite element simulations (Figure 3b; Figure S3, Supporting Information) as well as the reported theoretical behavior of shell-based spinodal topologies.[18] In the same relative density range, all other high-strength lattice materials have considerably less efficient scaling behavior, with scaling exponents of 1.9–2.5.[8,10] Similarly, in the catastrophic regime, we found $\sigma_c \sim \overline{\rho}^{2.47}$ and $E_c \sim \overline{\rho}^{2.27}$ for our nanospinodals. This is comparable to the theoretically predicted behavior of solid spinodal topologies, in which the solid phase is the direct result of a spinodal decomposition process.[18]
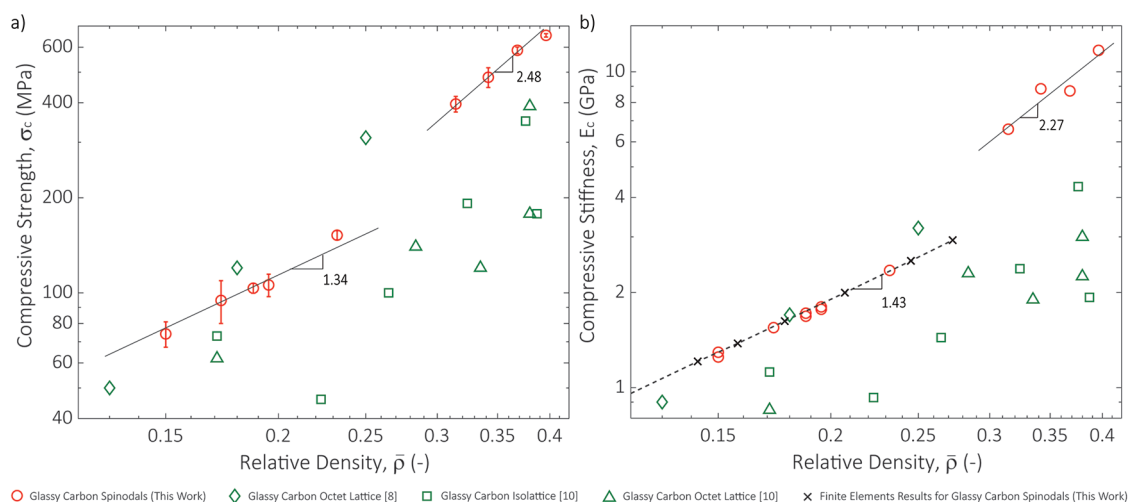
Figure 3. a) Compressive strength-versus-relative density and b) compressive stiffness-versus-relative density comparing glassy carbon nanospinodals of this study to glassy carbon beam-nanolattices.[8,10] Solid lines denote fits on the experimental data, while dashed lines correspond to finite element simulation results.

The observed transition from progressive to catastrophic failure in glassy carbon nanospinodals (Figures 1 and 2) can be explained by a shift in the propagation direction of emerging cracks within the shell, depending on the shell thickness-to-curvature radius ratio. To illustrate this, we consider a short section of spinodal shell, of thickness (t), curvature radius (R), and length of the order of the characteristic length scale of the spinodal topology (i.e., the unit cell size). For simplicity, we assume the Gaussian curvature to be equal to zero, so that plane strain conditions apply. **Figure 4** shows finite element simulations of the compression response of such idealized shells for different t/R ratios. For thin uncracked shells (Figure 4a), the maximum principal stress (in tension) is concentrated near the shell surface and oriented parallel to the loading direction; tensile stresses transverse to the loading direction are negligible. With increasing t/R, the maximum positive principal stress shifts to the inside of the shell and is now aligned transversally to the loading direction (Figure 4b,c). In a real shell, small cracks with random orientation may pre-exist throughout the structure. To investigate crack propagation, in Figure 4d–f we introduce two pre-existing cracks at locations corresponding to the two tensile stress maxima identified in Figure 4a–c. Crack A is at the outside fiber near the middle of the shell length, oriented transversely to the loading direction, and crack B is at the central fiber, near the top of the shell length and oriented parallel to the loading direction (Figure 4d). For thin shells (Figure 4d), crack A is under mode I loading and propagates transversally through the shell, whereas crack B is under compression and does not grow. Increasing t/R cause compression of crack A and propagation of crack B, which splits the shell longitudinally (Figure 4e,f). In all cases, cracks start to grow unstably at applied strains between 4% and 8%. Under shear loading (Figures S7 and S8, Supporting Information), only transverse crack propagation occurs, independent on the t/R ratio; furthermore, crack propagation requires substantially higher activation strains than under compression. This strongly suggests that the existence of the two failure regimes (progressive and catastrophic) is related to compressive failure of shell segments aligned with the loading direction.

These findings imply that sufficiently low-$\bar{\rho}$ spinodal structures under compression promote crack propagation transverse to the loading direction and impede crack growth along the loading direction. Although the shell sections of actual spinodal structures have various orientations with respect to an applied load, those aligned with the loading direction experience the highest compressive loads. In the progressive $\bar{\rho}$ regime, these shell sections crack transversally and only a small portion of the structure collapses and folds, then the mechanism starts again, leading to the layer-by-layer failure (Movie S1, Supporting Information). By contrast, higher $\bar{\rho}$ favor crack growth parallel to the loading direction within a percolating path of material, which can continue across the entire sample, thus inducing catastrophic failure (Movie S3, Supporting Information). Both cases are apparent from Figure 1, where the progressively failing structures gradually fracture into small pieces, whereas long fracture surfaces span across large parts of the structures in the catastrophic regime. Near the progressive-to-catastrophic failure transition $\bar{\rho}$ regime, both parallel and transverse crack growth may coexist for a certain time (Figure 1, $\bar{\rho} = 23\%$ and $\bar{\rho} = 31\%$; Figure 4e). In the progressive failure regime, increasing vertical crack formation does not lead to immediate failure; nonetheless, it causes more pronounced stress drops (Figure 2a). For the lower-$\bar{\rho}$ structures in the catastrophic failure regime, the limited number of progressive failure events before unstable vertical crack growth allow minor stress plateaus (Figure 2b). Depending on the first cracks to grow unstably, one propagation direction may eventually dominate (Figure 4), making for the sharp transition between progressive and catastrophic failure around $\bar{\rho} \approx 25\%$ (Figure 2c). The energy absorption efficiency (η) thereby quantifies the degree of catastrophic events (Figure S4a, Supporting Information), where all progressively failing structures reach high efficiencies, decreasing from 0.53 ($\bar{\rho} = 15\%$) to 0.36 ($\bar{\rho} = 23\%$), before sharply dropping to 0.04 ($\bar{\rho} \geq 31\%$) in the catastrophic regime.
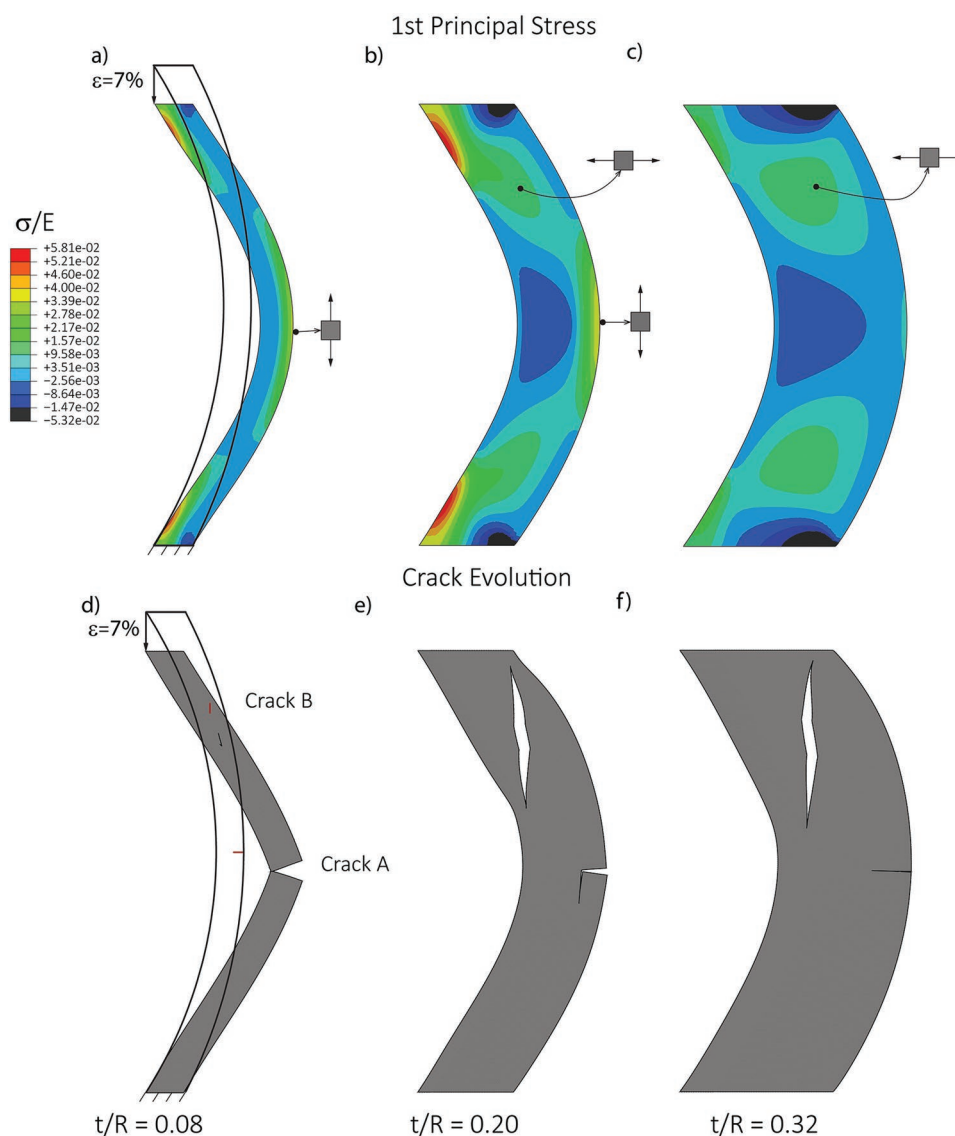
1st Principal Stress

Crack Evolution

Figure 4. Finite element simulations of the compression response of idealized spinodal shell cross-sections with different shell thickness-to-curvature radius ratios (t/R). a–c) First principal stress distribution in tension of uncracked models, insets mark the maximum values and indicate the stress direction. d–f) Crack evolution in precracked models.

In the progressive failure regime, an upper bound for the absorbed energy per unit volume can be approximated by the plateau stress (σ_{pl}) multiplied by the densification strain (ϵ_d), i.e., $U \sim \sigma_{pl}\epsilon_d \sim \overline{\rho}^{1.10}(1-1.4\overline{\rho}) \sim \overline{\rho}^{0.9}$, with the measured plateau strength scaling ($\sigma_{pl} \sim \overline{\rho}^{1.1}$, Figure S4b, Supporting Information). This is in good agreement with the nearly linear energy absorption scaling measured experimentally (Figure 2c). Conversely, assuming catastrophic, purely linear elastic behavior, the absorbed energy per unit volume can be estimated as $U \sim \frac{1}{2}\sigma_c^2/E_c \sim \overline{\rho}^{4.96}/\overline{\rho}^{2.27} \sim \overline{\rho}^{2.69}$, with the measured σ_c and E_c scalings; however, this rough estimate ignores energy absorption past the first stress drop, as observed for the lower-$\overline{\rho}$ structures in the catastrophic regime (Figure 2b), which explains the experimentally measured lower scaling exponent of 1.67.

The combination of optimized topology with an ultrastrong constituent material provides the superior energy absorption

capability of the glassy carbon nanospinodals presented herein, compared to other lattices and commercial materials (Figure 2d). Although beam-based lattices can be designed to possess high-strength, their sharply intersecting beams cause stress concentrations at the lattice nodes which serve as crack propagation sites,[6,18] potentially causing the generally observed catastrophic failure. By contrast, spinodal topologies are free of pronounced stress concentrations,[18] and as demonstrated above, crack propagation can be tailored by design, resulting in a very progressive failure mechanism. The high specific strength of nanoscale glassy carbon compared to most bulk materials may explain the superior energy absorption capability of our nanospinodals compared to larger-scale periodic shell-based structures with gyroid, p-Schwarz or other triply minimal surface topologies.[38,39] However, stochastic spinodal topologies where shown remarkably imperfection insensitive compared

to perfect shells, like thin walled cylinders,[18] and lack of periodicity has been shown to increase the damage tolerance of beam-based architectures;[40] this suggests that stochastic spinodals may also have topological advantages over periodic shell-based designs for crack deflection and progressive failure.

Despite being theoretically less efficient in terms of strength and stiffness, the presented nanospinodals compete very well with the most advanced beam-based lattices.[2,8,10] Assuming ideally pin-jointed nodes, strength and stiffness of beam-based trusses scale linearly with the relative density; in practice, nodes are rigid, and node bending as well as stress concentrations and imperfections often notably impair the actual scaling behavior and impose substantial knock-down factors to the theoretical predictions.[2,6,8,10] By contrast, stochastic spinodal structures have been shown to be very imperfection insensitive and the mechanical behavior reported here correlates well with the theoretical models (Figure 3b).[18] In particular, the strength of beam-based nanolattices quickly becomes buckling-limited when $\bar{\rho}$ is below 30%, due to the extremely high strength-to-Young's modulus ratio (σ/E) of the constituent material.[2] Assuming $\sigma/E \approx 1/10$ for the glassy carbon in this study,[2] the buckling regime of nanospinodals starts below $\bar{\rho} \approx 7\%$ (Figure S3, Supporting Information), again marking a considerable advantage of spinodal topologies over beam-based designs.

In summary, we show that nanospinodals, i.e., nanoarchitectures with spinodal shell topology, possess unprecedented combinations of high energy absorption, strength and stiffness at low density. This unique multifunctionality is attributed to three key features: (i) The nearly defect-free constituent glassy carbon material, with strengths on the order of the bulk theoretical limit; (ii) the efficient isotropic shell topology, characterized by near-zero mean curvature and negative Gaussian curvature; and (iii) a progressive failure mechanism that under compression comminutes the structures in a layer-by-layer fashion, preventing catastrophic failure. We explain this unique failure mechanism with a simple numerical model, showing that low shell thickness-to-curvature radius ratios impede the propagation of cracks that are aligned with the loading direction. Thus, with substantially higher specific energy absorption than any existing monolithic or architected material, yet ultrahigh strength and low weight, our glassy carbon nanospinodals demonstrate a level of multifunctionality which has not been shown in any other nanoarchitected material. Beyond what is demonstrated here, the ability to broadly vary the ratios of feature size and shell curvature of spinodal topologies, depending on the decomposition time at which geometries are extracted, may allow to further enhance multiple mechanical properties, such as the buckling resistance and imperfection sensitivity.[18] Furthermore, anisotropic spinodal designs allow optimization for a particular load case,[41] potentially improving single-axis performance compared to 2D structures like honeycombs.

Today, industrial application of architected materials (even with macroscopic topological features) is hindered by manufacturing limitations. By contrast, spinodal decomposition of a template material followed by material conversion may be a manufacturing route competitive with state-of-the-art foam production.[42–45] Nanospinodals have recently been demonstrated to be orders of magnitude more scalable than additively

manufactured nanolattices. Graphene and nickel nanospinodals with millimeter-size overall dimensions, yet nanometer-size features were fabricated via dealloying and polymeric Bijel templates, respectively.[44,45] The results of this study demonstrate that such spinodal architectures are an ideal platform for the next generation of superior cellular materials for structural applications and impact protection systems.

Experimental Section

Topology Generation: The spinodal shell topology was generated numerically in a two-step process.[18] (i) A solid-phase spinodal topology was generated via simulated spinodal-decomposition by solving the Cahn–Hilliard equation over a cubic domain with edge length (N), for two phases with equal volume fraction (see the Supporting Information).[46,47] Thereby, the selected decomposition time (t) at which the topology is extracted controls its shape, where increasing t lead to larger characteristic geometric feature sizes (λ) and smaller interface curvatures (see Figure S1, Supporting Information).[18] Here, t was adjusted to yield λ of 0.2N–0.25N, which has been shown to combine low imperfection sensitivity and high buckling-resistance.[18] (ii) The final shell spinodal topology was extracted from the contrast gradient of image slices of the two-phase solid, which were reduced to binary images via a threshold function.

Fabrication: Polymeric structures were printed on silicon substrates from the photoresist IP-Dip (Nanoscribe GmbH) using a Photonic Professional GT (Nanoscribe GmbH) DLW system. After DLW, samples were submerged in propylene glycol monomethyl ether acetate for 20 min, to dissolve uncured photoresist, followed by a 5 min long isopropanol bath for further cleaning. Subsequently, specimens were dried using an Autosamdri-931 (Tousimis Research Corp. Inc.) critical point dryer. The polymeric specimens were then pyrolyzed to glassy carbon at 900 °C in a vacuum tube furnace (see Figure S2, Supporting Information).[8,10] Adjusting the structure-size-to-shell-thickness ratio of the polymeric templates resulted in 13–6 µm size glassy carbon nanospinodals with 0.17–0.3 µm thick shells and $\bar{\rho}$ = 15–40%, respectively.

Experimental Characterization: Specimen dimensions were optically measured using an FEI Magellan 400XHR (Thermo Fisher Scientific Inc.) scanning electron microscope (SEM). To determine the mechanical properties of glassy carbon nanospinodals, uniaxial compression experiments were performed at a constant strain rate of 0.001 s^{-1} using a FT-NMT03 (FemtoTools AG) nanomechanical testing system equipped with an FT-S200 sensor and an Alemnis nanoindenter (Alemnis AG) with a flat punch diamond tip, 100 µm in diameter. Load–displacement curves were recorded, and the displacement was corrected for equipment and substrate compliances via a digital image correlation algorithm developed in house. Three samples per each density were tested. Applying the measured dimensions, engineering stress and strain were determined. Compressive stiffness (E_c) and strength (σ_c) were extracted as the maximum slope in the linear elastic regime and the maximum engineering stress before densification, respectively. The plateau stress is calculated as the average compressive stress between initial failure and densification.[48] Relative ($\bar{\rho}$) and effective densities (ρ) were determined by CAD models and SEM measured dimensions, with a density of glassy carbon of 1.3–1.5 g cm^{-3}.[49,50] The energy absorption per unit volume (U) was calculated as the area under the stress–strain curve until catastrophic failure or until the densification strain $\varepsilon_d = 1 - 1.4\bar{\rho}$,[51] whichever occured first. The specific energy absorptions ($\bar{U}$) is given by $\bar{U} = U/\rho$.

Finite Element Analysis: Finite element simulations were carried out in ABAQUS (Dassault Systèmes SE). E_c and σ_c of glassy carbon nanospinodals were simulated using shell elements (S3R) in geometrically nonlinear analyses, with an elastic perfectly plastic constituent material, with a Young's modulus of 34 GPa (see Figure S5, Supporting Information) and a yield stress of 3.4 GPa.[52] The models were fixed on bottom surfaces, free at their sides, and subjected to a

uniform vertical displacement on the top surfaces, matching the experimental conditions. For the crack propagation analysis, a nonlinear eXtended finite element method analysis with plane stress quadratic elements (CPS4R) with a constant element size between the different t/R models was used. The models were deformed until the first crack fully propagated. To account for mesh sensitivity, analyses with two different mesh sizes, with 100 and 200 elements per the model length (L), respectively (8 and 16 across t for the thinnest cross-section), were performed and the same results were obtained. Linear elastic material behavior, with a Young's modulus of 34 GPa, and a crack propagation stress of 500 MPa was applied. See Figure S6 of the Supporting Information for boundary conditions and geometrical details.

Supporting Information

Supporting Information is available from the Wiley Online Library or from the author.

Conflict of Interest

The authors declare no conflict of interest.

[1] N. A. Fleck, V. S. Deshpande, M. F. Ashby, *Proc. R. Soc. A* **2010**, *466*, 2495.

[2] J. Bauer, L. R. Meza, T. A. Schaedler, R. Schwaiger, X. Zheng, L. Valdevit, *Adv. Mater.* **2017**, *29*, 1701850.

[3] G. Lu, T. X. Yu, *Energy Absorption of Structures and Materials*, CRC Press, Boca Raton, FL **2003**.

[4] T. A. Schaedler, A. J. Jacobsen, A. Torrents, A. E. Sorensen, J. Lian, J. R. Greer, L. Valdevit, W. B. Carter, *Science* **2011**, *334*, 962.

[5] K. J. Maloney, C. S. Roper, A. J. Jacobsen, W. B. Carter, L. Valdevit, T. A. Schaedler, *APL Mater.* **2013**, *1*, 022106.

[6] L. R. Meza, S. Das, J. R. Greer, *Science* **2014**, *345*, 1322.

[7] L. Salari-Sharif, T. A. Schaedler, L. Valdevit, *J. Mater. Res.* **2014**, *29*, 1755.

[8] J. Bauer, A. Schroer, R. Schwaiger, O. Kraft, *Nat. Mater.* **2016**, *15*, 438.

[9] J. J. do Rosário, J. B. Berger, E. T. Lilleodden, R. M. McMeeking, G. A. Schneider, *Extreme Mech. Lett.* **2017**, *12*, 86.

[10] X. Zhang, A. Vyatskikh, H. Gao, J. R. Greer, X. Li, *Proc. Natl. Acad. Sci. USA* **2019**, *116*, 6665.

[11] A. Misra, J. R. Raney, L. De Nardo, A. E. Craig, C. Daraio, *ACS Nano* **2011**, *5*, 7713.

[12] H. Hu, Z. Zhao, W. Wan, Y. Gogotsi, J. Qiu, *Adv. Mater.* **2013**, *25*, 2219.

[13] O. Al-Ketan, R. Rezgui, R. Rowshan, H. Du, N. X. Fang, R. K. Abu Al-Rub, *Adv. Eng. Mater.* **2018**, *20*, 1800029.

[14] J. B. Berger, H. N. G. Wadley, R. M. McMeeking, *Nature* **2017**, *543*, 533.

[15] T. Tancogne-Dejean, M. Diamantopoulou, M. B. Gorji, C. Bonatti, D. Mohr, *Adv. Mater.* **2018**, *30*, 1803334.

[16] S. C. Han, J. W. Lee, K. Kang, *Adv. Mater.* **2015**, *27*, 5506.

[17] S. Rajagopalan, R. Robb, *Med. Image Anal.* **2006**, *10*, 693.

[18] M.-T. Hsieh, B. Endo, Y. Zhang, J. Bauer, L. Valdevit, *J. Mech. Phys. Solids* **2019**, *125*, 401.

[19] J. W. Cahn, *Acta Metall.* **1961**, *9*, 795.

[20] H. Jinnai, T. Koga, Y. Nishikawa, T. Hashimoto, S. T. Hyde, *Phys. Rev. Lett.* **1997**, *78*, 2248.

[21] G. C. Jacob, J. F. Fellers, S. Simunovic, J. M. Starbuck, *J. Compos. Mater.* **2002**, *36*, 813.

[22] J. J. do Rosário, E. T. Lilleodden, M. Waleczek, R. Kubrin, A. Yu. Petrov, P. N. Dyachenko, J. E. C. Sabisch, K. Nielsch, N. Huber, M. Eich, G. A. Schneider, *Adv. Eng. Mater.* **2015**, *17*, 1420.

[23] M. Mieszala, M. Hasegawa, G. Guillonneau, J. Bauer, R. Raghavan, C. Frantz, O. Kraft, S. Mischler, J. Michler, L. Philippe, *Small* **2017**, *13*, 1602514.

[24] A. Schroer, J. M. Wheeler, R. Schwaiger, *J. Mater. Res.* **2018**, *33*, 274.

[25] L. Xiao, W. Song, *Int. J. Impact Eng.* **2018**, *111*, 255.

[26] I. Maskery, N. T. Aboulkhair, A. O. Aremu, C. J. Tuck, I. A. Ashcroft, R. D. Wildman, R. J. M. Hague, *Mater. Sci. Eng., A* **2016**, *670*, 264.

[27] S. Y. Choy, C.-N. Sun, K. F. Leong, J. Wei, *Mater. Des.* **2017**, *131*, 112.

[28] L. Yang, R. Mertens, M. Ferrucci, C. Yan, Y. Shi, S. Yang, *Mater. Des.* **2019**, *162*, 394.

[29] D. S. J. Al-Saedi, S. H. Masood, M. Faizan-Ur-Rab, A. Alomarah, P. Ponnusamy, *Mater. Des.* **2018**, *144*, 32.

[30] M. Zhao, F. Liu, G. Fu, D. Zhang, T. Zhang, H. Zhou, *Materials* **2018**, *11*, 2411.

[31] L. Zhang, S. Feih, S. Daynes, S. Chang, M. Y. Wang, J. Wei, W. F. Lu, *Addit. Manuf.* **2018**, *23*, 505.

[32] I. Maskery, N. T. Aboulkhair, A. O. Aremu, C. J. Tuck, I. A. Ashcroft, *Addit. Manuf.* **2017**, *16*, 24.

[33] C. Bonatti, D. Mohr, *Acta Mater.* **2019**, *164*, 301.

[34] T. A. Schaedler, C. J. Ro, A. E. Sorensen, Z. Eckel, S. S. Yang, W. B. Carter, A. J. Jacobsen, *Adv. Eng. Mater.* **2014**, *16*, 276.

[35] A. G. Evans, J. W. Hutchinson, M. F. Ashby, *Prog. Mater. Sci.* **1998**, *43*, 171.

[36] J. Bauer, S. Hengsbach, I. Tesari, R. Schwaiger, O. Kraft, *Proc. Natl. Acad. Sci. USA* **2014**, *111*, 2453.

[37] J. Miltz, G. Gruenbaum, *Polym. Eng. Sci.* **1981**, *21*, 1010.

[38] H. A. Schwarz, *Gesammelte Mathematische Abhandlungen*, Springer, Berlin **1890**.

[39] A. H. Schoen, *Infinite Periodic Minimal Surfaces without Self-Intersections*, National Aeronautics And Space Administration, Washington, DC **1970**.

[40] M.-S. Pham, C. Liu, I. Todd, J. Lertthanasarn, *Nature* **2019**, *565*, 305.

[41] A. Vidyasagar, S. Krödel, D. M. Kochmann, *Proc. R. Soc. A* **2018**, *474*, 20180535.

[42] E. M. Herzig, K. A. White, A. B. Schofield, W. C. K. Poon, P. S. Clegg, *Nat. Mater.* **2007**, *6*, 966.

[43] M. N. Lee, A. Mohraz, *Adv. Mater.* **2010**, *22*, 4836.

[44] J. A. Witt, D. R. Mumm, A. Mohraz, *J. Mater. Chem. A* **2016**, *4*, 1000.

[45] H. Kashani, Y. Ito, J. Han, P. Liu, M. Chen, *Sci. Adv.* **2019**, *5*, eaat6951.

[46] X.-Y. Sun, G.-K. Xu, X. Li, X.-Q. Feng, H. Gao, *J. Appl. Phys.* **2013**, *113*, 023505.

[47] J. W. Cahn, J. E. Hilliard, *J. Chem. Phys.* **1958**, *28*, 258.

[48] Y. Liu, T. A. Schaedler, A. J. Jacobsen, X. Chen, *Composites, Part B* **2014**, *67*, 39.

[49] F. C. Cowlard, J. C. Lewis, *J. Mater. Sci.* **1967**, *2*, 507.

[50] O. J. A. Schueller, S. T. Brittain, C. Marzolin, G. M. Whitesides, *Chem. Mater.* **1997**, *9*, 1399.

[51] L. J. Gibson, M. F. Ashby, *Cellular Solids: Structure and Properties*, Cambridge University Press, Cambridge **1997**.

[52] A. Albiez, R. Schwaiger, *MRS Adv.* **2019**, *4*, 133.